光学学报

7×1中红外光纤合束器的设计、制备与性能

黄梓轩[1]，王虎[1]，祁思胜[2]，顾晓南[1]，李森森[3]，杨安平[1]，冯宪[1]，田康振[1*]，杨志勇[1,2**]

[1]江苏师范大学物理与电子工程学院江苏省先进激光材料与器件重点实验室，江苏 徐州 221116；

[2]中国科学院上海光学精密机械研究所中国科学院强激光材料重点实验室，上海 201800；

[3]光电信息控制和安全技术重点实验室，天津 300308

摘要 中红外光纤合束器可将多个低功率的中红外激光器进行合束，从而实现较高的功率输出。本工作研制了一种7×1硫系玻璃光纤合束器（未熔接输出光纤），评估了其中红外传输特性。该光纤合束器由$As_{40}S_{60}$/$As_{38}S_{62}$光纤组束熔融拉锥而成，初始光纤的纤芯直径和包层直径分别为200 μm和250 μm，数值孔径为0.38～0.35(@2～6 μm)，拉锥比例R为3和4，锥形过渡区长度为2 cm。测试结果表明：当$R=3$时，制备的光纤合束器在3 μm和4.6 μm波长的端口传输效率分别为>90%和>87%；当$R=4$时，制备的光纤合束器在3 μm和4.6 μm波长的端口传输效率分别为>88%和>85%；光纤合束器输出端的光纤单丝之间未发生明显串扰。

关键词 材料；硫系玻璃光纤；光纤合束器；中红外；端口传输效率

中图分类号 TN213 **文献标志码** A **DOI:** 10.3788/AOS230775

1 引 言

中红外波段一般指2～20 μm波段，该波段包含3～5 μm和8～12 μm两个大气低损耗窗口，且涵盖大量气体、化学和生物分子的指纹吸收谱，因此中红外激光技术在环境监测、医疗健康等领域具有重大应用价值。中红外激光光源主要有固体激光器[1-2]、气体激光器[3-4]、光学参量振荡器(OPO)[5-6]、量子级联激光器(QCL)[7-8]、光纤激光器[9-11]等。其中，QCL具有体积小、质量轻、结构紧凑等特点，是目前覆盖波长范围最宽(3～13 μm)的小型可实用中红外激光器。但单个QCL的输出功率有限，至今报道的最高输出功率为～8 W[12]。激光合束被认为是显著提高QCL输出功率的有效途径，该技术通过将多个激光器的输出功率进行叠加实现较高的功率水平。与光谱合束、相干合束等空间合束技术相比，光纤合束技术无需自由空间光学元件，具有结构紧凑、鲁棒性好的优点，被认为是中红外QCL提升功率的优选技术。

光纤合束技术通过将N根光纤组合拉锥实现合束，这样形成的光纤器件称为N×1光纤合束器。中红外光纤合束器一般采用硫系玻璃光纤或氟化物玻璃光纤通过熔融拉锥方法制备。2013年，Gattass等[13]制备了7×1 As-S硫系光纤合束器，端口传输效率>76%@2 μm。2019年，Major等[14]制备7×1 As-Se硫系光纤合束器，用其将4个不同波段QCL合束，获得6.02～11.17 μm宽波段激光输出。2022年，Annunziato等[15]制备了3×1 InF_3基氟化物光纤合束器，端口传输效率>77%@1.55 μm。与氟化物玻璃光纤（光谱范围为0.5～5 μm）相比，硫系玻璃光纤具有更宽的光谱范围（硫化物光纤1～6.5 μm[16-17]，硒化物光纤1.5-9 μm[18-19]，碲化物光纤3～12 μm[18,20]）以及更好的热稳定性和化学稳定性，利于宽波段、高传输效率中红外光纤合束器的制备。本文设计和制备了一种具有高传输效率(>85%@3～5 μm)的7×1中红外硫系玻璃光纤合束器，并研究了其中红外传输特性。

2 实 验

2.1 样品制备

本研究选取As-S硫系玻璃材料制备光纤合束器，因为该玻璃具有极好的抗析晶热稳定性和较高的激光损伤阈值[21-22]。纤芯和包层玻璃的化学组成分别为$As_{40}S_{60}$和$As_{38}S_{62}$，它们可在300 ℃附近拉制成光纤[22]。7×1光纤合束器的制备过程如图1所示，包括高纯玻璃的制备、光纤的制备、毛细管制备、光纤组束拉锥、光纤锥区切割和光纤合束器铠装。

As-S硫系玻璃的制备采用真空熔融-淬冷法[22-23]，所用原料为7N纯度的As和6N纯度的S。配料前，将As在320 ℃真空处理1 h除去原料表面可能存在的氧

收稿日期：2023-04-04；**修回日期**：2023-05-30；**录用日期**：2023-09-04；**网络首发日期**：2023-09-14

基金项目：国家自然科学基金(62175096,U21A2056)、国防科技重点实验室基金(6142107200315)

通信作者：*kangzhentian@jsnu.edu.cn；**yangzhiyong@jsnu.edu.cn

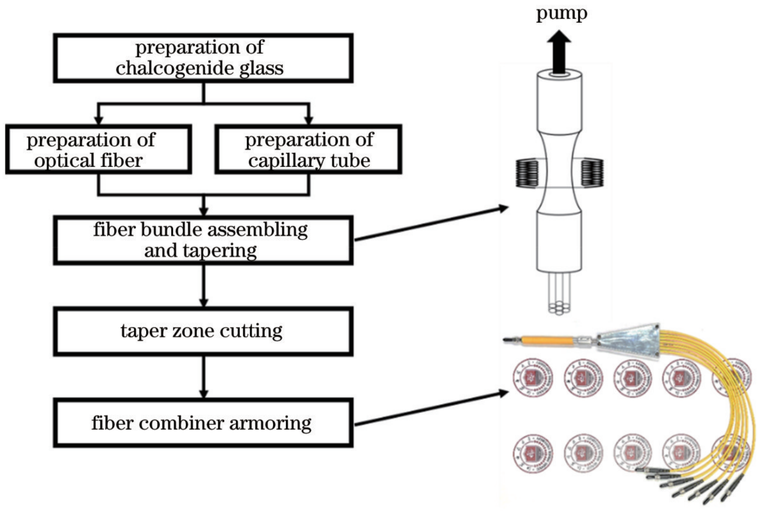

图1　7×1硫系玻璃光纤合束器制备过程示意图

Fig. 1　Schematic of fabrication process of 7×1 chalcogenide glass fiber combiner

化物杂质，将S真空蒸馏4次尽可能去除其中的C和H杂质。As-S光纤的制备采用棒管法，芯棒为使用内径15 mm的石英管制备的Φ14.9 mm×120 mm $As_{40}S_{60}$玻璃棒，包层套管为使用内径19 mm石英管通过真空旋管技术制备的$As_{38}S_{62}$玻璃管（外径18.9 mm，内径15 mm，长度120 mm）。将芯棒插入包层套管，然后包裹约1 mm厚度的热塑性聚醚酰亚胺（PEI）薄膜形成光纤预制棒，最后放入软玻璃光纤拉丝塔的气氛保护加热炉中，在300 ℃附近拉制成直径约270 μm的光纤。$As_{38}S_{62}$毛细管的制备采用挤压和热拉制相结合的方法，首先采用挤压技术[24]将Φ30 mm×30 mm的抛光玻璃片挤压成内外径分别为4.8 mm和12 mm的玻璃管，然后在300 ℃附近拉制成内外径分别为0.76 mm和1.9 mm的毛细管。光纤组束拉锥过程在自制的纵向拉锥系统上完成：首先取7根长度约50 cm的光纤，将光纤一端约8 cm浸入二甲基乙酰胺（DMAC）溶剂中溶解掉光纤表面的聚合物；然后将无聚合物光纤端插入长度约12 cm的$As_{38}S_{62}$毛细管中，并使用高温胶将毛细管与光纤胶合；之后将连接毛细管的光纤束置于纵向拉锥系统的管式炉中，该拉锥系统为自搭建设备，包括电阻加热器、真空系统、拉锥动力系统等。将毛细管无光纤一端与真空泵连接使毛细管内处于真空状态（如图1所示）。然后，在270 ℃附近拉锥，采用恒力拉锥的方式，拉力为~0.2 N。随后，在拉锥后的光纤束的锥区进行切割，获得光纤合束器（未熔接输出光纤）。最后，将光纤合束器铠装。

2.2　样品表征

玻璃的红外透过光谱采用Bruker Tensor 27傅里叶变换红外光谱仪（FTIR）测试。玻璃在2~12 μm的线性折射率采用椭偏技术测试，测试设备和方法与文献[25-26]相同。光纤的传输损耗采用截断法测得，测试设备为配备外置光纤耦合装置和液氮制冷HgCdTe探测器的上述FTIR。

光纤合束器的端口传输效率测试方法如图2(a)所示，红外光源为Light Conversion Orpheus-HP光学参量放大器（OPA），输出激光经CaF_2全息偏振片和CaF_2聚焦透镜进入光纤合束器的单根光纤中，使用Thorlabs S180C探测器（工作波段2.9~5.5 μm）测试输入和输出端的激光功率P_{in}和P_{out}。端口传输效率通过式(1)计算：

$$\eta = \frac{P_{in}}{\alpha P_{out}}, \tag{1}$$

式中：α为光纤耦合效率，可用截断法测得。该端口传输效率是将光纤两个端面反射去除后的结果，即包含光纤传输损耗而不包含端面反射的内部透过率。光纤合束器输出端的光斑远场测量方法如图2(b)所示，其光纤输入端耦合光路与图2(a)相同，光纤输出端光斑采用Dataray WinCamD-IR-BB中红外光束质量分析仪（工作波段2~16 μm）观测。

3　分析与讨论

图3(a)为$As_{40}S_{60}$和$As_{38}S_{62}$玻璃的红外透过光谱，它们在2~8 μm波段内显示出良好的透射性能，在4.0 μm波长附近的微弱吸收与玻璃中残余的S-H杂质有关，在2.9 μm和4.3 μm波长附近的微弱吸收分别与玻璃中残余或空气中的OH/H_2O和CO_2有关。图3(b)为$As_{40}S_{60}$和$As_{38}S_{62}$玻璃的折射率色散曲线，它们对应的Sellmeier方程分别为

$$n^2_{As_{40}S_{60}} = 1 + \frac{4.8255\lambda^2}{\lambda^2 - 0.2564^2} + \frac{1.0210\lambda^2}{\lambda^2 - 29.38^2}, \tag{2}$$

$$n^2_{As_{38}S_{62}} = 1 + \frac{4.6982\lambda^2}{\lambda^2 - 0.2254^2} + \frac{1.0700\lambda^2}{\lambda^2 - 31.52^2}, \tag{3}$$

式中，λ为波长。可以看出，二者在2~6 μm波段的折射率差Δn为0.03~0.026。以$As_{40}S_{60}$和$As_{38}S_{62}$玻璃分别作为纤芯和包层材料，可以制备出数值孔径（NA）

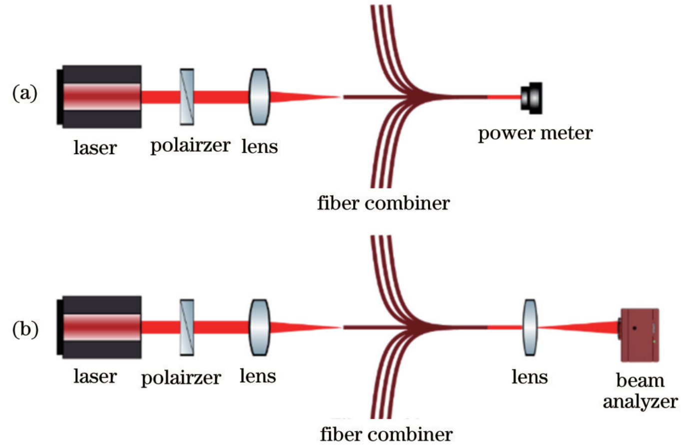

图 2 硫系光纤合束器的测试实验装置示意图。(a)端口传输效率；(b)输出光斑

Fig. 2 Experimental setup for measuring of chalcogenide fiber combiner. (a) Port transmission efficiency; (b) output spot

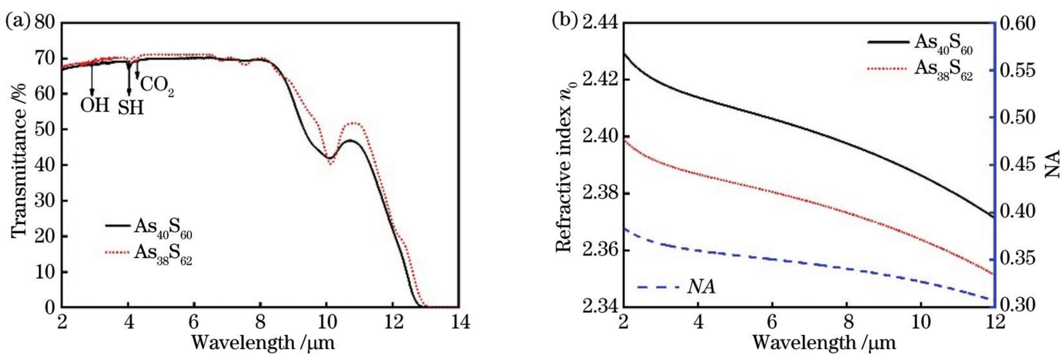

图 3 As-S 玻璃的透过光谱、线性折射率和光纤的 NA。(a)透过光谱；(b)线性折射率和光纤的 NA

Fig. 3 Transmission spectra, linear refractive indices of As-S glasses and the calculated NA of the fiber. (a) Transmission spectra; (b) linear refractive indices and the calculated NA of the fiber

为 0.38～0.35(@2～6 μm)的光纤，如图 3(b)所示。

图 4 为拉制的直径约为 270 μm 光纤的传输损耗，插图为溶掉聚合物后的光纤截面图，纤芯和包层直径分别为 200 μm 和 250 μm。光纤在 2～7 μm 波段的损耗曲线采用 FTIR 测得，在 3 μm 和 4.6 μm 波长的损耗采用 OPA 作为光源测得，光纤的初始长度约为 3 m，每次截取 0.4～1 m。可以看出，该光纤在 2～6.5 μm 波段具有较好的传输性能，其背景损耗约为 0.5 dB/m，在 3 μm 和 4.6 μm 波长的损耗分别为 (0.56±0.04) dB/m 和 (0.63±0.05) dB/m。光纤在 4～4.3 μm 表现出较高的损耗，这与光纤中残留的 S-H 和 CO_2 杂质有关[22, 27]。

基于玻璃的折射率和光纤的尺寸设计 7×1 光纤合束器，主要探索合适的合束锥区的过渡区长度和锥腰直径。7 根光纤采用紧密堆积方式，如图 5(a)所示。图 5(b)为采用光线追迹理论研究光在一段拉锥光纤中传输的示意图，其中，D 为拉锥前光纤直径，d 为拉锥后光纤直径，R_{in} 和 R_{out} 分别为拉锥前后光纤纤芯半径，L 为锥形过渡区长度，φ 和 θ 为光线入射角及光线进入光纤后的折射角，φ_1 和 φ_2 分别为第 1 次和第 2 次在纤芯-包层分界面上的反射角。对于 N×1 光纤合束

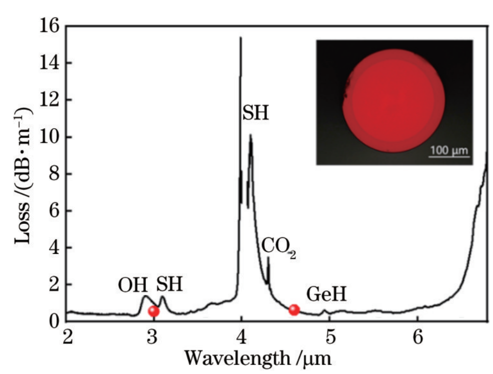

图 4 As-S 光纤的传输损耗，插图为光纤的横截面

Fig. 4 Attenuation of fabricated As-S fiber, the inset shows the cross section of the fiber

器，从其输出端可承受的激光功率和输出光斑大小方面考虑，选择其拉锥缩小比 R 在 $\sqrt{N}$ 附近。本研究对 R 为 2～4 时不同 Δn(纤芯和包层折射率差)对应的临界 L(满足绝热拉锥所需最短锥形过渡区长度)进行了计算[28-29]：

$$L \geqslant \frac{(R_{in} - R_{out})\cos\theta}{\frac{R_{out}}{R_{in}}\left[1-\left(\frac{n_{clad}}{n_{core}}\right)\right]-\sin\theta}, \tag{4}$$

式中，n_{core}和n_{clad}分别为纤芯和包层玻璃的折射率。计算结果如图 6 所示，可以看出，当Δn为 0.02～0.04、R为 2～4 时，临界L均小于 500 μm。考虑到锥区的锥度可能存在波动，同时为了更好地将各被激发模式的能量约束在纤芯内，实验中采用的L比计算的临界值大 20～40 倍。

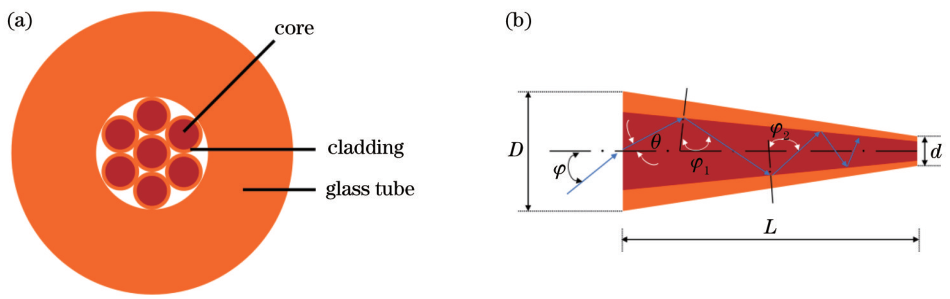

图 5　光纤合束器设计示意图。(a)紧密堆积的 7×1 光纤合束器横截面示意图；(b)光在拉锥光纤中传输示意图

Fig. 5　Design diagram of the fiber combiner. (a) Schematic cross section of 7×1 fiber combiner formed by tightly packed fibers; (b) schematic diagram of light transmission in tapped fiber

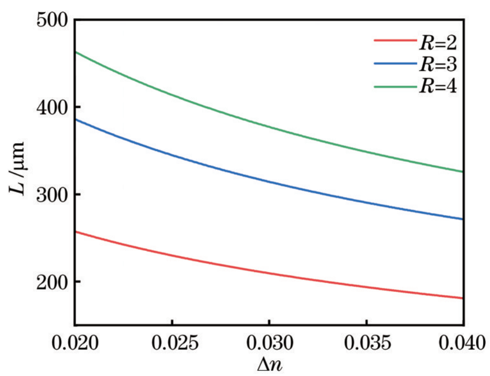

图 6　对于不同拉锥比例R，锥形过渡区长度L的临界值与Δn的关系

Fig. 6　The relationship between critical L and Δn for different taper ratio R

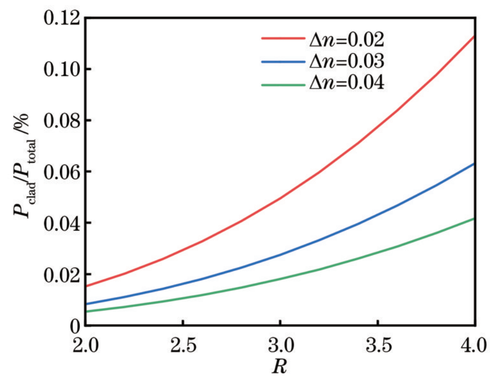

图 7　对于不同拉锥比例R，光纤纤芯光场能量泄漏进入包层的比值P_{clad}/P_{total}与Δn的关系

Fig. 7　The relationship between P_{clad}/P_{total} and Δn for different taper ratio R

对于光纤合束器，由于输出端光纤单丝的纤芯尺寸被缩小，其纤芯支持的高阶模数减少，这些模式的能量被耦合到低阶模中或者被泄漏到包层中，而泄漏到包层的光场能量会被束缚在包层中或者被耦合到近邻光纤中引起串扰。因此，拉锥比例R和Δn对泄漏到包层的光场能量均会产生影响。图 7 为不同R时从光纤纤芯泄漏进入包层的光场能量比值(P_{clad}/P_{total})随Δn的变化。可以看到：P_{clad}/P_{total}随着R的增大而增大；对于R为 2～4 的光纤合束器，当$\Delta n \geqslant 0.02$时，可以有效地将P_{clad}/P_{total}控制在 0.12% 以下。在实际情况中，由于制备的硫系光纤为支持几百个高阶模的多模光纤，光场能量在各个模式中的分配取决于耦合条件和光纤所处的状态(如弯曲、应力等)，更多的光场能量倾向于被耦合于较低阶的模式中。

根据上述光纤合束器的设计，拉制了R分别为 3 和 4 的 7×1 光纤合束器，锥形过渡区长度L约为 2 cm。图 8 为制备的光纤合束器输出端截面图，可以看出，光纤单丝呈较好的正六边形排列，其在拉锥后未发生显著形变。选取 3 μm 和 4.6 μm 两个波长进行端口传输效率η测试，测试结果如表 1 所示。当$R=3$时，光纤合束器在 3 μm 波长的η为 90.7%～92.5%，在 4.6 μm 波长的η为 87.2%～90.8%。当$R=4$时，光纤合束器的η有所下降，在 3 μm 和 4.6 μm 波长的η分别为 88.1%～91.4% 和 85.1%～87.5%。制备的光纤合束器在 3 μm 波长的η高于其在 4.6 μm 波长的η，这与光纤在 3 μm 具有较低的损耗有关；与$R=3$时相比，光纤合束器在$R=4$时表现出较低的η，这可能与后者较细的单丝导致泄漏到光纤包层中的光场能量较多有关。

为了评估光纤合束器输出端光纤单丝间是否存在串扰，将中红外激光依次耦合进输入端的光纤单丝中，使用红外光束质量分析仪对输出光斑进行观测，结果如图 9 所示。对于$R=3$和$R=4$对应的光纤合束器，均未观察到光纤单丝间的串扰。为了评估激光经过合束器后光束质量的变化，采用聚焦光束法对经过单根光纤和经过合束器的激光光束质量(M^2)进行测量，所用激光波长为 3 μm，M^2约为 1.5。相关结果如图 10 所示，测得激光经过芯径 200 μm 单根光纤后的M^2约为 12，经过合束器中单根拉锥光纤后($R=3$)的M^2约

为8。可以看到，光束质量有所提高，较高阶的模式在合束部分被转换成了较低阶的模式。由于实验条件的限制，本研究尚未使用制备的光纤合束器对多个低功率激光器进行合束。

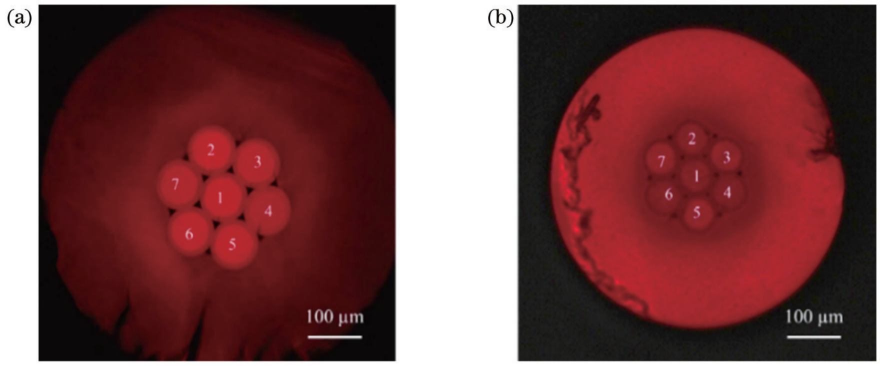

图8　制备的光纤合束器的输出端照片。(a) R=3；(b) R=4

Fig. 8　Images of the output end of fabricated fiber combiner. (a) R=3; (b) R=4

表1　制备的光纤合束器(未熔接输出光纤)在3 μm和4.6 μm的端口传输效率

Table 1　Port transmission efficiencies of fabricated 7×1 fiber combiner (without fusing output fiber) measured at 3 μm and 4.6 μm

R	Wavelength /μm	Port transmission efficiency /%							
		1	2	3	4	5	6	7	Average
3	3	92.5	90.7	91.8	91.1	92.2	90.8	91.5	91.5
	4.6	90.8	87.2	90.4	88.4	90.1	88.1	89.1	89.2
4	3	91.4	88.1	90.1	89.8	90.9	88.7	90.5	89.9
	4.6	87.5	85.1	87.1	85.9	87.2	85.4	86.8	86.4

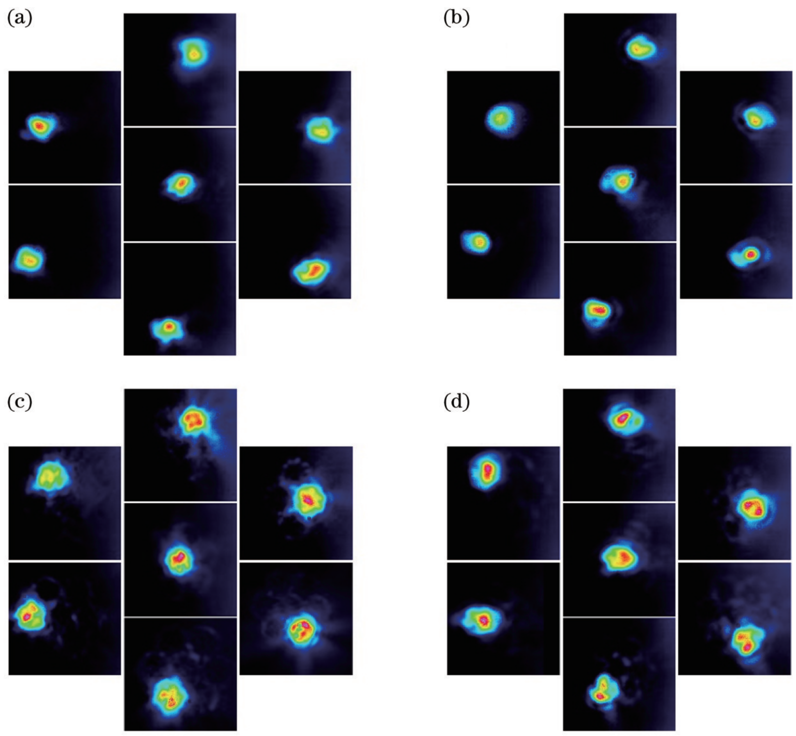

图9　将光耦合进R=3和R=4对应的光纤合束器各端口光纤中时拍摄的输出光斑。(a) R=3，3 μm；(b) R=3，4.6 μm；(c) R=4，3 μm；(d) R=4，4.6 μm

Fig. 9　The captured light spots at the output end of the fiber combiner with R=3 and R=4. (a) R=3, 3 μm; (b) R=3, 4.6 μm; (c) R=4, 3 μm; (d) R=4, 4.6 μm

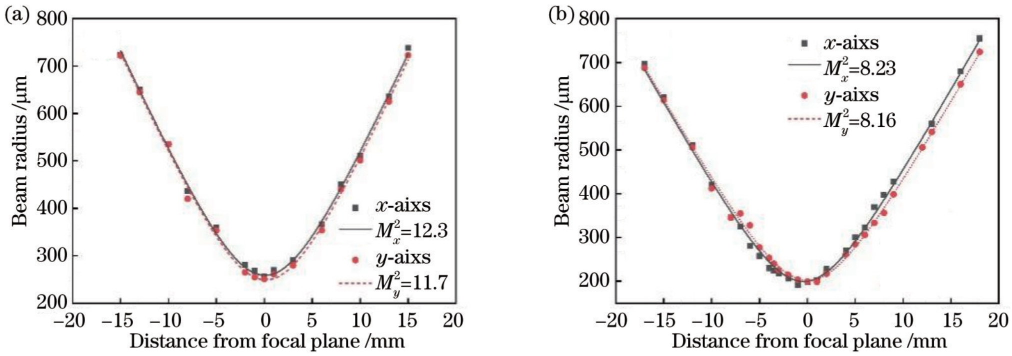

图10 光束质量M^2。(a)激光通过单根多模光纤后的光束质量M^2;(b)激光通过合束器中单根拉锥光纤后的光束质量M^2

Fig. 10 Beam quality M^2. (a) The beam quality M^2 of the laser after passing through a single multimode fiber; (b) the beam quality M^2 of the laser after passing through a single tapered fiber in the combiner

4 结 论

以$As_{40}S_{60}$和$As_{38}S_{62}$硫系玻璃分别为纤芯和包层材料可制备出芯径为200 μm、包层直径为250 μm、NA为0.38~0.35(@2~6 μm)的硫系玻璃光纤。当拉锥比例R约为3、锥形过渡区长度>500 μm时，$As_{40}S_{60}$/$As_{38}S_{62}$光纤合束器理论上具有较高的传输效率。采用熔融拉锥技术分别制备出R=3和R=4(锥形过渡区长度均为2 cm)的7×1光纤合束器(未熔接输出光纤)，前者在3 μm和4.6 μm波长的端口传输效率分别为>90%和>87%，后者在3 μm和4.6 μm波长的端口传输效率略低，分别为>88%和>85%，制备的光纤合束器输出端的光纤单丝间无明显串扰。这些结果表明，制备的光纤合束器是一种较高效的激光合束器件，有望用于中红外激光(如QCL)功率提升、中红外宽光谱合成等领域。

参 考 文 献

[1] Lü Z, Shen Y, Zong N, et al. 1.53 W all-solid-state nanosecond pulsed mid-infrared laser at 6.45 μm[J]. Optics Letters, 2022, 47(6): 1359-1362.

[2] Scott P. Mid-infrared lasers[J]. Nature Photonics, 2010, 4(8): 576-577.

[3] 崔宇龙，周智越，黄威，等. 中红外光纤激光技术研究进展与展望[J]. 光学学报, 2022, 42(9): 0900001.
Cui Y L, Zhou Z Y, Huang W, et al. Progress and prospect of mid-infrared fiber laser technology[J]. Acta Optica Sinica, 2022, 42(9): 0900001.

[4] 黄威，周智越，崔宇龙，等. 4.5 W中红外3.1 μm光纤气体激光器[J]. 中国激光, 2022, 49(1): 0101024.
Huang W, Zhou Z Y, Cui Y L, et al. 4.5 W 3.1 μm mid-infrared fiber gas laser[J]. Chinese Journal of Lasers, 2022, 49(1): 0101024.

[5] Hu S W, Wang L, Guo Y W, et al. High-conversion-efficiency tunable mid-infrared $BaGa_4Se_7$ optical parametric oscillator pumped by a 2.79-μm laser[J]. Optics Letters, 2019, 44(9): 2201-2203.

[6] Yuan J H, Li C, Yao B Q, et al. High power, tunable mid-infrared $BaGa_4Se_7$ optical parametric oscillator pumped by a 2.1 μm Ho: YAG laser[J]. Optics Express, 2016, 24(6): 6083-6087.

[7] Yao Y, Hoffman A J, Gmachl C F. Mid-infrared quantum cascade lasers[J]. Nature Photonics, 2012, 6(7): 432-439.

[8] Zhao G, Tian J F, Hodges J T, et al. Frequency stabilization of a quantum cascade laser by weak resonant feedback from a Fabry-Perot cavity[J]. Optics Letters, 2021, 46(13): 3057-3060.

[9] Coco M G, Aro S C, McDaniel S A, et al. Continuous wave Fe^{2+}: ZnSe mid-IR optical fiber lasers[J]. Optics Express, 2020, 28(20): 30263-30274.

[10] Yao C F, Jia Z X, Li Z R, et al. High-power mid-infrared supercontinuum laser source using fluorotellurite fiber[J]. Optica, 2018, 5(10): 1264-1270.

[11] Yue W J, Ding Y C, Wu B, et al. High-power mid-infrared picosecond pulse bunch generation through difference frequency generation[J]. Optics Letters, 2020, 45(2): 383-386.

[12] Zhou W J, Lu Q Y, Wu D H, et al. High-power, continuous-wave, phase-locked quantum cascade laser arrays emitting at 8 μm[J]. Optics Express, 2019, 27(11): 15776-15785.

[13] Gattass R R, Shaw L B, Kung F H, et al. Infrared fiber N×1 multimode combiner[J]. IEEE Photonics Journal, 2013, 5(5): 7100905.

[14] Major K J, Shaw L B, Busse L, et al. Fiber optic coupled quantum cascade infrared laser system for detection of explosive materials on surfaces[J]. Optics & Laser Technology, 2019, 119: 105635.

[15] Annunziato A, Anelli F, du Teilleul P L P, et al. Fused optical fiber combiner based on indium fluoride glass: perspectives for mid-IR applications[J]. Optics Express, 2022, 30(24): 44160-44174.

[16] 田康振，胡永胜，任和，等. 高激光损伤阈值Ge-As-S硫系玻璃光纤及中红外超连续谱产生[J]. 物理学报, 2021, 70(4): 047801.
Tian K Z, Hu Y S, Ren H, et al. Ge-As-S chalcogenide glass fiber with high laser damage threshold and mid-infrared supercontinuum generation[J]. Acta Physica Sinica, 2021, 70(4): 047801.

[17] Zhang H, Chang Y J, Xu Y T, et al. Design and fabrication of a chalcogenide hollow-core anti-resonant fiber for mid-infrared applications[J]. Optics Express, 2023, 31(5): 7659-7670.

[18] Tao G M, Ebendorff-Heidepriem H, Stolyarov A M, et al. Infrared fibers[J]. Advances in Optics and Photonics, 2015, 7(2): 379.

[19] Zhang B, Guo W, Yu Y, et al. Low loss, high NA chalcogenide glass fibers for broadband mid-infrared supercontinuum generation[J]. Journal of the American Ceramic Society, 2015, 98(5): 1389-1392.

[20] Wang X G, Zhao Z M, Wang X S, et al. Mid-infrared supercontinuum generation in low-loss single-mode Te-rich chalcogenide fiber[J]. Optical Materials Express, 2019, 9(8): 3487-3493.

[21] You C Y, Dai S X, Zhang P Q, et al. Mid-infrared femtosecond laser-induced damages in As_2S_3 and As_2Se_3 chalcogenide glasses

[J]. Scientific Reports, 2017, 7: 6497.

[22] Qi S S, Li Y B, Huang Z X, et al. Flexible chalcogenide glass large-core multimode fibers for hundred-watt-level mid-infrared 2-5 μm laser transmission[J]. Optics Express, 2022, 30(9): 14629-14644.

[23] Hu Y S, Tian K Z, Li T T, et al. Mid-infrared nonlinear optical performances of Ge-Sb-S chalcogenide glasses[J]. Optical Materials Express, 2021, 11(3): 695-706.

[24] Ren H, Yu Y, Zhai C C, et al. Chalcogenide glass fibers with a rectangular core for polarized mid-infrared supercontinuum generation[J]. Journal of Non-Crystalline Solids, 2019, 517: 57-60.

[25] 米浩婷, 杨安平, 黄梓轩, 等. Ga_2S_3-Sb_2S_3-Ag_2S 硫系玻璃和光纤的制备及性能研究[J]. 物理学报, 2023, 72(4): 047101.
Mi H T, Yang A P, Huang Z X, et al. Preparation and properties of Ga_2S_3-Sb_2S_3-Ag_2S chalcogenide glasses and optical fibers[J]. Acta Physica Sinica, 2023, 72(4): 047101.

[26] Yang Y, Yang Z Y, Lucas P, et al. Composition dependence of physical and optical properties in Ge-As-S chalcogenide glasses [J]. Journal of Non-Crystalline Solids, 2016, 440: 38-42.

[27] Zhang M J, Li L, Li T T, et al. Mid-infrared supercontinuum generation in chalcogenide fibers with high laser damage threshold[J]. Optics Express, 2019, 27(20): 29287-29296.

[28] 刘文博. 单模—多模光纤合束器的传输特性研究[D]. 长沙: 国防科学技术大学, 2015: 15-16.
Liu W B. Study on transmission characteristics of single-mode-multimode fiber combiner[D]. Changsha: National University of Defense Technology, 2015: 15-16.

[29] Birks T A, Li Y W. The shape of fiber tapers[J]. Journal of Lightwave Technology, 1992, 10(4): 432-438.

Design, Fabrication, and Properties of 7×1 Mid-Infrared Fiber Combiner

Huang Zixuan[1], Wang Hu[1], Qi Sisheng[2], Gu Xiaonan[1], Li Sensen[3], Yang Anping[1], Feng Xian[1], Tian Kangzhen[1*], Yang Zhiyong[1,2**]

[1]*Jiangsu Key Laboratory of Advanced Laser Materials and Devices, School of Physics and Electronic Engineering, Jiangsu Normal University, Xuzhou* 221116, *Jiangsu, China*;

[2]*Key Laboratory of Materials for High-Power Laser, Shanghai Institute of Optics and Fine Mechanics, Chinese Academy of Sciences, Shanghai* 201800, *China*;

[3]*Science and Technology on Electro-Optical Information Security Control National Key Laboratory, Tianjin* 300308, *China*

Abstract

Objective In recent years, mid-infrared lasers have caught increasing attention because of their significant applications in a number of fields such as defense security, environment monitoring, and medical surgery. They mainly include solid state laser, gas laser, optical parametric oscillator, quantum cascade laser (QCL), and fiber laser. Among them, since QCL features small size, lightweight, and ultra-wide wavelength coverage (3–13 μm commercially available currently), it is considered a promising compact and practical mid-infrared laser. However, the output power of a single QCL is limited to 10 W level. Laser beam combining technology is considered an effective way to significantly improve the output power of QCL. In this technology, a higher power level is achieved by superposing the output power of multiple lasers. Compared with spatial beam-combining technologies such as spectral beam combining and coherent beam combining, optical fiber beam-combining technology has the advantages of compact structure and good robustness, and is the preferred technology for improving the output power of QCL. Thus, we aim to develop a compact mid-infrared combiner for the power enhancement of QCL.

Methods As-S chalcogenide glass is employed to fabricate the optical fiber combiner because of its excellent thermal stability against crystallization and relatively high laser damage threshold. The chemical compositions of the core and cladding glass are $As_{40}S_{60}$ and $As_{38}S_{62}$ respectively. The fabrication of 7×1 fiber combiner includes the preparation of high-purity glass, optical fiber, and capillary tube, fiber bundle assembling and tapering, taper zone cutting, and fiber combiner armoring. The $As_{40}S_{60}$ and $As_{38}S_{62}$ chalcogenide glasses are prepared in low-OH quartz tubes by the vacuum melt-quenching method. The As-S optical fiber is fabricated by the rod-in-tube method, the cladding tube is by the rotational method, and the $As_{38}S_{62}$ capillary tube is by the combination of extrusion and thermal-drawing methods. The fiber bundle tapering is conducted on a self-made longitudinal tapering system. First, seven fibers with a length of about 50 cm are cut out, and one end of the fiber (about 8 cm long) is immersed in dimethylacetamide (DMAC) solvent to dissolve the surface polymer. The polymer-free ends of the seven fibers are then inserted into the $As_{38}S_{62}$ capillary tube with a length of about 12 cm, and the capillary tube is glued with the fiber bundle using a high-temperature adhesive. Subsequently, the fiber bundle is placed into the tube furnace of the longitudinal tapering system, the fiber-free end of the capillary tube is connected to a vacuum pump to maintain lower pressure inside the capillary tube, and the fiber bundle is tapered at about

270 ℃. Finally, the tapered region of the fiber bundle is cut and the obtained fiber combiner (without fusing output fiber) is armored.

Results and Discussions The fabricated $As_{40}S_{60}/As_{38}S_{62}$ fiber has a core diameter of 200 μm and a cladding diameter of 250 μm. It shows good transmission performance in the 2-6.5 μm with a background loss of about 0.5 dB/m. The losses at 3 μm and 4.6 μm are (0.56±0.04) dB/m and (0.63±0.05) dB/m respectively. Based on the fabricated fiber, the 7×1 fiber combiner is designed. The numerical simulation shows that the appropriate taper reduction ratio R is 2-4, and the length of the taper transition zone should be more than 500 μm. Following the design, 7×1 fiber combiners with R of 3 and 4 are fabricated (Fig. 8). The taper transition zone is about 2 cm long. The cross-sectional images of the output end of the fiber combiners show that the fiber monofilaments are arranged in a good regular hexagonal shape, and the fiber bundles do not undergo significant deformation after being tapered. The measurements show that the port transmission efficiency η of the fiber combiner is 90.7%-92.5% at 3 μm and 87.2%-90.8% at 4.6 μm when $R=3$, and it is 88.1%-91.4% and 85.1%-87.5% at 3 μm and 4.6 μm respectively when $R=4$ (Table 1).

Conclusions We develop a 7×1 chalcogenide glass fiber combiner and investigate its mid-infrared transmission properties. The fiber combiner is formed by fusing and tapering an $As_{40}S_{60}/As_{38}S_{62}$ fiber bundle. The core and cladding diameters of the individual fiber are 200 μm and 250 μm respectively, with the numerical aperture of 0.38-0.35 (@ 2-6 μm). The taper ratio R of the final fiber combiner is 3 or 4, and the length of the taper transition zone is about 2 cm. The results show that when $R=3$, the port transmission efficiency of the fabricated fiber combiner at 3 μm and 4.6 μm is more than 90% and 87% respectively, and when $R=4$, it is more than 88% and 85% respectively. There is no obvious crosstalk between the fiber monofilament at the output end of the fiber combiner. The results indicate that the fabricated fiber combiner is an efficient laser combining device and is promising in mid-infrared laser power enhancement and wide spectrum synthesis.

Key words materials; chalcogenide glass fiber; fiber combiner; mid-infrared; port transmission efficiency